Hindawi
Advances in Meteorology
Volume 2017, Article ID 1042603, 15 pages
https://doi.org/10.1155/2017/1042603

Research Article

Quantifying Spatiotemporal Dynamics of Solar Radiation over the Northeast China Based on ACO-BPNN Model and Intensity Analysis

Xiangqian Li, Zhijun Tong, Enliang Guo, and Xiaolong Luo

School of Environment, Northeast Normal University, Changchun 130117, China

Correspondence should be addressed to Zhijun Tong; gis@nenu.edu.cn

Received 9 May 2017; Revised 5 July 2017; Accepted 19 July 2017; Published 24 August 2017

Academic Editor: Harry D. Kambezidis

Reliable information on the spatiotemporal dynamics of solar radiation plays a crucial role in studies relating to global climate change. In this study, a new backpropagation neural network (BPNN) model optimized with an Ant Colony Optimization (ACO) algorithm was developed to generate the ACO-BPNN model, which had demonstrated superior performance for simulating solar radiation compared to traditional BPNN modelling, for Northeast China. On this basis, we applied an intensity analysis to investigate the spatiotemporal variation of solar radiation from 1982 to 2010 over the study region at three levels: interval, category, and conversion. Research findings revealed that (1) the solar radiation resource in the study region increased from the 1980s to the 2000s and the average annual rate of variation from the 1980s to the 1990s was lower than that from the 1990s to the 2000s and (2) the gains and losses of solar radiation at each level were in different conditions. The poor, normal, and comparatively abundant levels were transferred to higher levels, whereas the abundant level was transferred to lower levels. We believe our findings contribute to implementing ad hoc energy management strategies to optimize the use of solar radiation resources and provide scientific suggestions for policy planning.

1. Introduction

Solar radiation is one of the most renewable and sustainable energy sources for the Earth's ecosystem, affecting nearly all physical, chemical, and biological processes on the planet [1–3]. Its spatiotemporal variation on the Earth's surface directly determines the formation and evolution of climate [4, 5]. Therefore, complete and accurate information on the spatiotemporal dynamics of solar radiation has been the focus of global climate change studies during the past several decades [6–8].

However, solar radiation observation sites are relatively sparse compared to conventional weather stations that measure conventional meteorological parameters (i.e., temperature and precipitation); this may be attributed to the equipment and maintenance costs [9]. This imposes a significant issue and serious hindrance to forming a better understanding of the variations in solar radiation, especially in developing countries. To that end, high precision models for simulating solar radiation at low costs are imperative, and utilizing easily accessible meteorological variables and available tools is an effective way to achieve this goal. According to the literature, we can summarize four main types of models for estimating solar radiation: (1) radiative transfer models, (2) climatic empirical models, (3) remote sensing-based models, and (4) artificial intelligence models. Radiative transfer models take into account the effects of physical factors (e.g., scattering of atmospheric molecules and aerosols and absorption of carbon dioxide and ozone absorption) and meteorological factors (e.g., cloud amount and sunshine hours) on solar radiation, which make for strong physical attribute characterization architecture. Spectral radiation models and broadband radiation models are representative theoretical models [10–20]. Nevertheless, the structures of these classical models are fairly complex. In addition, some input parameters (e.g., ozone thickness and atmospheric precipitable water) are difficult to acquire at large scales. These disadvantages confine the application of

theoretical models. The climate empirical models mainly utilize conventional weather observation data such as sunshine percentage, cloud amount, and temperature to establish empirical formulas, which have been extensively used in simulating solar radiation due to the convenient calculations and relatively high precision. Angstrom-Prescott and Hargreaves-Samani models are common climate empirical models [21–23]; however, these are difficult to apply universally as their empirical coefficients usually change with time and place. Artificial intelligence models, in particular the widely used back propagation (BP) neural network (BPNN), have made significant contributions to the study of solar radiation simulations [24–28]. BPNN has the ability of self-organization, self-adaptation, and self-learning, which avoids the complex process of analyzing data and constructing model as it summarizes the experience and reduces error from human interpretation [29]. Additionally, its ability to adaptively process information can be used to address the complex input-output nonlinear mapping problem, especially regarding fuzzy information problems that require simultaneous consideration of many factors and imprecise conditions [30]. The causes of solar radiation variations are quite complicated as there are many meteorological elements that contribute to its value [31–33]. In general, using the BPNN model to simulate solar radiation is a better method to overcome the existing problems. Nevertheless, the traditional BPNN model has its own limitations, such as a slower convergence rate and easily defaulting into a local optimal solution. Consequently, we propose ACO-BPNN, a modified BPNN model optimized by an ant colony algorithm, to overcome those disadvantages.

To date, almost all studies on spatiotemporal solar radiation variation adopt climatological statistical diagnosis methods such as the empirical orthogonal function, wavelet analysis, and the Mann-Kendall test. These were designed to detect spatial patterns, periodic regularity, and abrupt point, respectively [34–36]. Although these methods could quantitatively analyze the spatiotemporal characteristics of solar radiation to some extent, they could not reveal the dynamic process of changes in solar radiation and reflect dynamic conversion regularity between different levels of solar radiation over the study region. Hence, it is necessary to introduce a new method to improve analysis for the spatiotemporal dynamics of regional solar radiation. In recent years, the intensity analysis method has been applied to land use and land cover change research, which can fully apply transfer matrix to analyze the intensity of land changes at three levels during different time periods: time interval, categories, and conversion [37]. There is no doubt that we will have a clearer understanding of the spatiotemporal dynamics of solar radiation if the precisely simulated characteristics of the ACO-BPNN model are combined with the dynamic analysis ability of intensity analysis.

Northeast China (NEC), known as a region very sensitive to global climate change [38–40], has suffered enormous economic losses due to frequent and increasing natural disasters (i.e., floods, droughts, and soil erosion) [41–43]. Restoring vegetation and carrying out sustainable agriculture have become necessary for ecological remediation and the sustainable development of the economy in this region. Solar radiation is necessary for the growth of vegetation; therefore, it is critical to quantitatively analyze its spatiotemporal variation to implement proper and reasonable vegetation restoration plans and agricultural ecological patterns. However, the majority of previous studies regarding estimating solar radiation over NEC adopted climate empirical models and solar radiative models, and dynamic changes in solar radiation of this region were limited to traditional trend analyses that did not reflect the continuous, dynamic changes [44–46]. Therefore, the main objectives of this study were to (1) estimate solar radiation over NEC using the ACO-BPNN model and (2) apply the intensity analysis method to characterize the dynamic variations in solar radiation of this region.

2. Materials and Methods

2.1. Study Area Description. The NEC region, spanning approximately 1.24 million km^2 (15.32% of the total area of China), and located between 38°42′–53°35′N and 115°25′–135°09′E (Figure 1), was selected as the study area of interest. It starts from the ChangBai Mountains in the east, reaches the Greater Khingan Mountains in the west, borders the Bohai Sea in the south, and extends to the Lesser Khingan Mountains in the north. These mountain ranges surround the central plains, including the Liao River Plain and the Songnen Plain. The Sanjiang Plain is located in the northeast corner of NEC, and the central plains constitute the Northeast Plain that is a significant marketable grain base. The NEC region lies in the east coast of Eurasia and thus is sensitive to the activity and intensity of a temperate monsoon climate. The annual precipitation varies from 400 mm in the northwest to 1,000 mm in the southeast and is concentrated mostly in summer (50–70%), with approximately equal amounts occurring in spring and autumn and the least amount occurring in the winter. The annual mean temperature ranges from −5.5°C in the northwest to 11.5°C in the southeast.

2.2. Data Collection and Preparation. For a better understanding of the spatiotemporal dynamics of solar radiation, data on meteorological observations and solar radiation of NEC were collected from the China National Meteorological Centre (CNMC), including monthly sum values of air temperature (at), wind speed (ws), vapor pressure (vp), relative humidity (rh), cloud amount (ca), sunshine duration (sd), and daily temperature range (dtr). Data from 1982 to 2010 were initially included from 131 meteorological stations distributed over the entire NEC region. Solar radiation data from 18 radiation stations also adopted monthly sum values (MJ/m^2). The longitude, latitude, and elevation above sea level of all stations were also recorded; as these stations were established at different years, some stations are missing data and therefore the records are of different lengths. To ensure consistency of the data series, meteorological data sets from a total of 114 stations, including 18 stations with radiation observations and 96 stations without them, were finally adopted for analysis, covering a period of 29 years from January 1982 to December 2010.

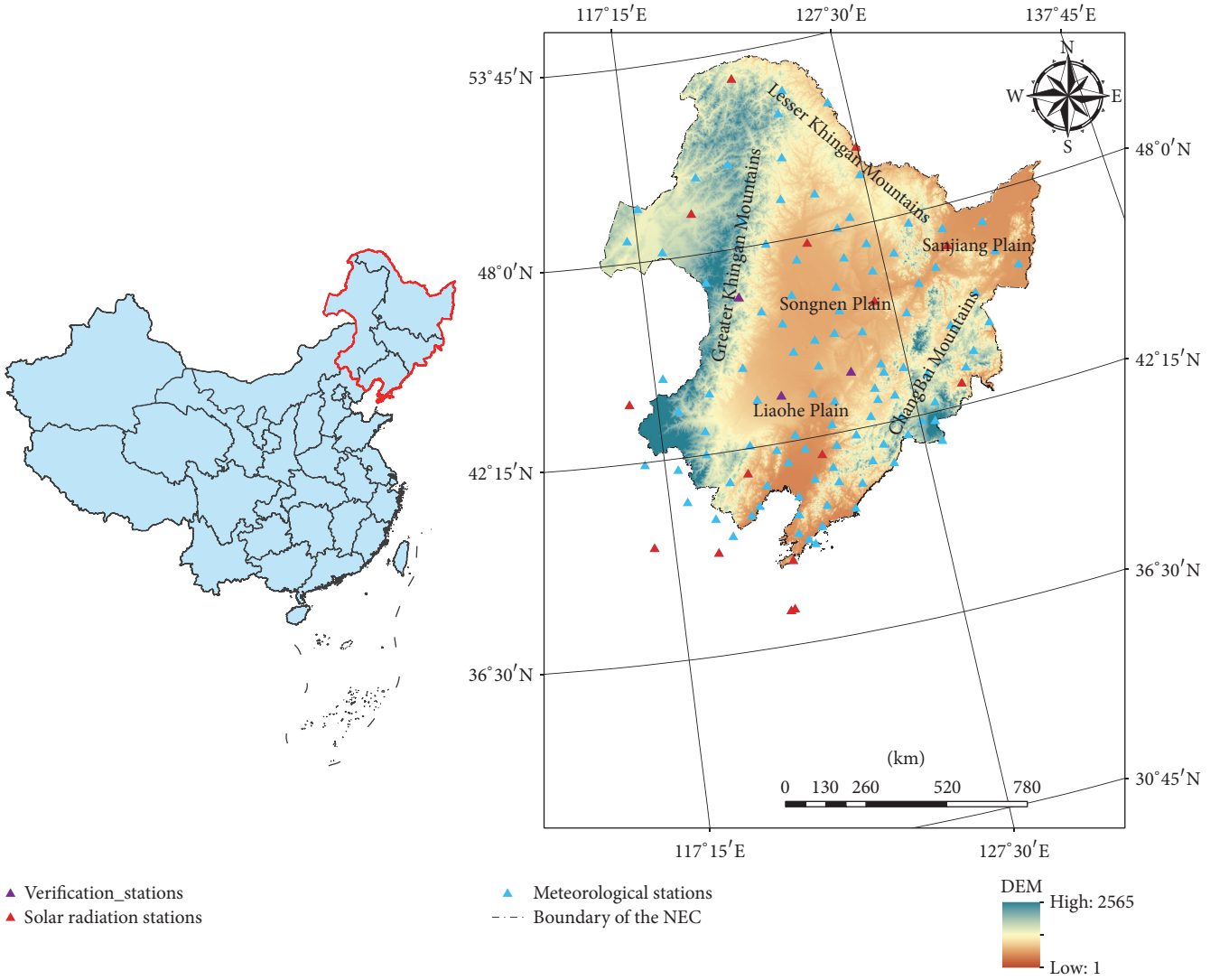

Figure 1: Map of the study area, Northeast China.

The data sequence was reviewed to ensure that there were no missing data, and three radiation stations (SuoLun, TongLiao, and ChangChun) were chosen as the verification points. Therefore, these stations were not involved in the establishment of the ACO-BPNN model.

2.3. Models

2.3.1. Overview of the BPNN Model. The BPNN is named after the back propagation (BP) algorithm, which is a typical multilayer network including the input layer, hidden layer, and the output layer. Hecht Nielsen proved that the 3-layer feedforward network with one hidden layer could approximate any multivariate function [47]. Therefore, BPNNs usually adopt 3-layer structures, and higher fitting precision can be obtained by adding the number of neurons in each layer. Moreover, the model adopts full connection between layers, and there is no connection between the same layer neurons (Figure 2).

The BP algorithm aims to minimize the total error of the network by feeding back the results of the learning to the hidden layer neurons to adjust the weights. The specific algorithm is as follows:

$$\begin{aligned} \text{net}_j &= \sum_i w_{ij} x_i + \Theta_j, \\ y_j &= f\left(\text{net}_j\right), \end{aligned} \tag{1}$$

where x_i is the output value of the previous node i; w_{ij} is the connection weights; Θ_j is the threshold of unit j, generally between -1 and 1; and f usually adopts a Sigmoid-type activation function:

$$f(a) = \frac{1}{1 + e^{-a}}. \tag{2}$$

For a training sample, the error between actual output and expected output is defined as follows:

$$E = \frac{1}{2} \sum_{k=1}^{l} \left(t_k - o_k\right)^2, \tag{3}$$

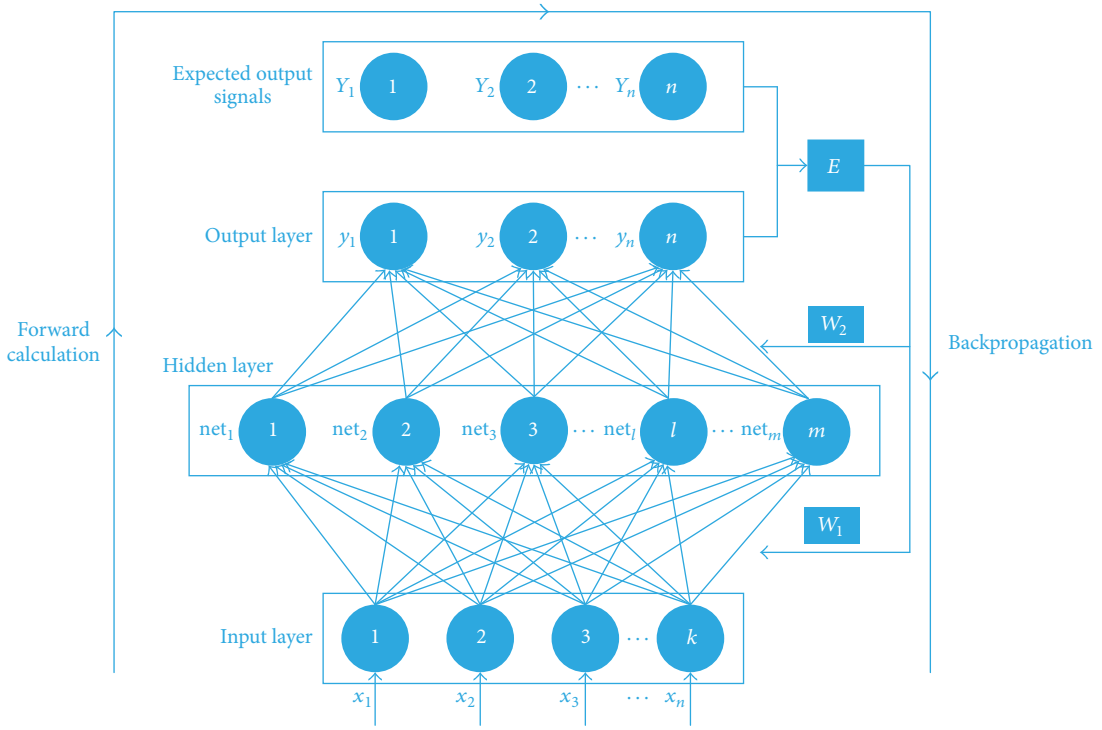

Figure 2: Backpropagation neural network with three layers.

where l is the number of output layer units; t_k is the expected output of unit k of output layer; o_k is the actual output of unit k of output layer.

The time required to process all training samples is referred to as a cycle. When training a multilayer neural network, the BP algorithm often can make the error E less than the specified threshold set by researchers after a number of cycles. At this point, the network achieves convergence and ends the iterative training process.

2.3.2. Incorporating ACO into the BPNN. Due to simple principles and strong operability, the BP algorithm has been used extensively in a large number of research fields. However, the BP algorithm also revealed some disadvantages with its popularization. In essence, the BP algorithm is a gradient descent algorithm that will significantly reduce the speed of model convergence when the objective function approaches the optimal value. If the initial parameter values are not properly set, the algorithm easily falls into a local optimum. By contrast, the Ant Colony Optimization (ACO) algorithm simulates the mode of an ant colony in finding the optimal foraging path, which is characterized by an intelligent universal search optimization ability and a more robust performance [48]. Therefore, in this study, an ACO algorithm was chosen to offer several optimized groups of initial weight values for the BPNN, which is then further refined to the most appropriate weights. The BPNN not only maintains the nonlinear mapping ability of the network but also possesses the universal optimization ability.

To apply the ACO algorithm to the network, the definition domains of all parameters consisting of weights and thresholds were separated into a series of discrete points. Consequently, each point was an optional value for the corresponding parameter. Once an ant was determined, it can only select a value for each parameter from numerous optional points and records its counter mark concurrently. In other words, each parameter required a corresponding pheromone table (Table 1).

Table 1: Pheromone table for each parameter.

	w_i			
Tag	1	2	⋯	n
Dividing calibration	a_1	a_2	⋯	a_n
Pheromone amount	$\tau(1)$	$\tau(2)$	⋯	$\tau(n)$

In Table 1, w_i is the ith parameter to be optimized, a_i is the dividing calibrated value that can be seen as a point, $\tau(i)$ represents the pheromone amount of point a_i, and n is the number of optional points. So the domain was divided into $n-1$ parts.

When the kth ant reached the parameter w_i, it selected the point value according to the probability that can be calculated by the following formula:

$$P_k(i) = \frac{\tau_i}{\sum_{1 \le j \le m} \tau_j}. \quad (4)$$

After selecting values for all the parameters, the kth ant accomplishes a traversal. Then it returns to the original nest

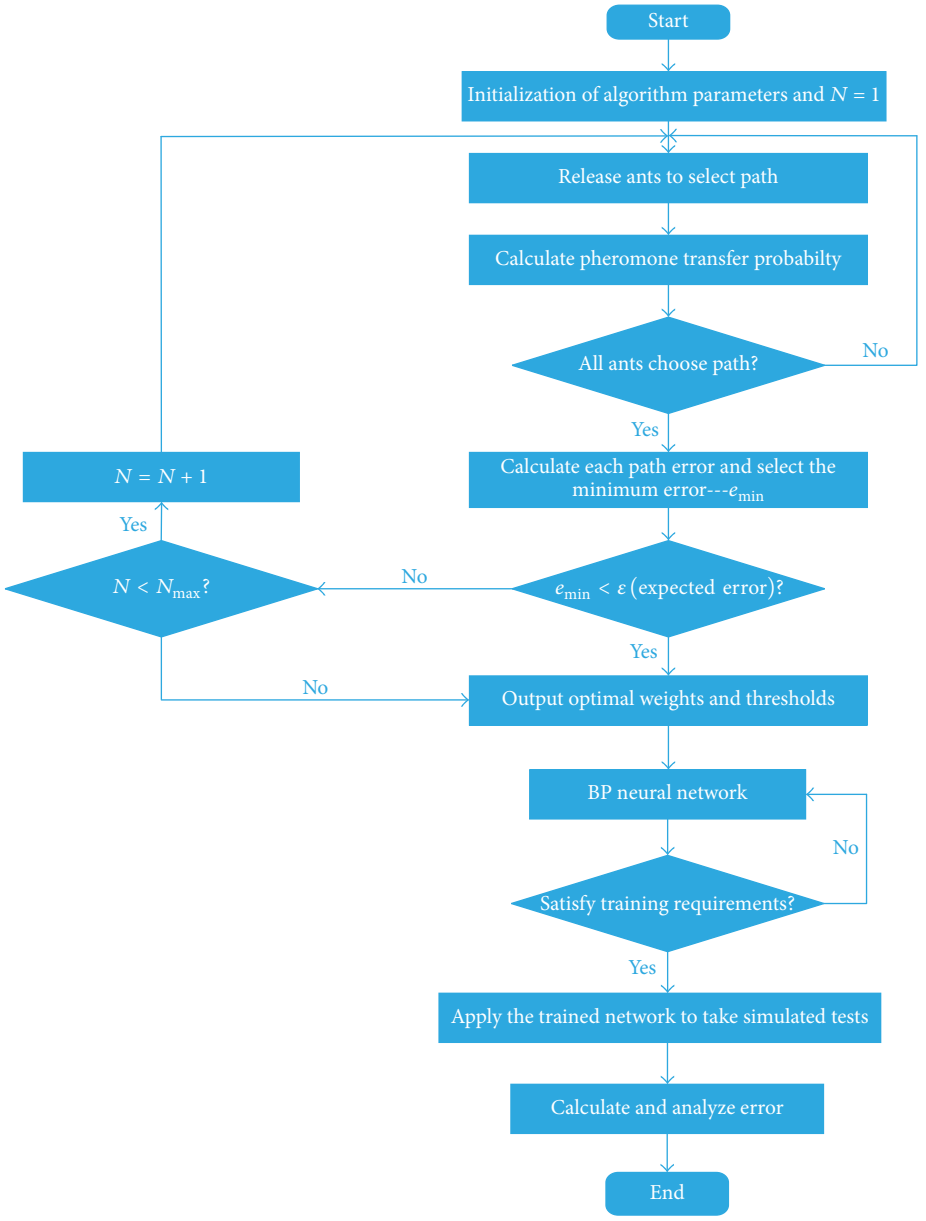

Figure 3: The flow chart of the improved BPNN: ACO-BPNN model.

and updates the pheromone table concurrently through the following equation:

$$\tau(i+1) = (1-\rho)\tau(i) + \Delta\tau(i), \tag{5}$$

where ρ is the evaporation coefficient of pheromone, which ranges from 0 to 1. $\Delta\tau(i)$ refers to a pheromone increase, which can be obtained based on the following equation:

$$\Delta\tau(i) = \frac{Q}{\mathrm{Er}}, \tag{6}$$

where Q denotes the pheromone quantity, which is a constant. Er is the error between the actual output and expected output.

When all ants finished selecting values, a better combination of parameters for neural network was obtained. However, it was determined that the output precision of the neural network was relatively low when these parameters were directly applied, which may have been attributed to the fact that the definition domain was split into a series of discrete points. Therefore, a further searching algorithm, BP, was required to improve accuracy and facilitate the neural network in achieving rapid convergence. However, the BP algorithm provided random values for initializing the neural network parameters, which increased the risk of being trapped into the local optimum. We took full advantage of the ACO to provide a more suitable group of initial weight values for the BPNN. As a result, the speed of convergence and output precision was advanced. The framework of the ACO-BPNN model is displayed in Figure 3.

2.3.3. Error Analysis Methods. In this study, the mean absolute percentage error (MAPE), mean absolute biased error (MABE), and root mean square error (RMSE) were employed to analyze the error between measured and simulated radiation values. MAPE, MABE, and RMSE most often reflected the comprehensive condition, long term fitting performance, and sensitivity and short-term fitting information of the model. The formulas to calculate them are as follows:

$$\begin{aligned} \mathrm{MAPE} &= \frac{1}{N}\sum_{i=1}^{N}\left(\frac{S_m - S_r}{S_r}\right), \\ \mathrm{MABE} &= \frac{1}{N}\sum_{i=1}^{N}\left(S_m - S_r\right), \\ \mathrm{RMSE} &= \sqrt{\sum_{i=1}^{N}\frac{\left(S_m - S_r\right)^2}{N}}, \end{aligned} \tag{7}$$

where S_m represents the simulated value of the monthly sum of solar radiation, S_r represents the actual value of monthly solar radiation, and N refers to the number of samples.

2.4. Spatial Interpolation Method. Spatial interpolation was performed to provide a monthly spatial distribution of the dynamic analysis for the solar radiation across the NEC region from 1982 to 2010. Here the inverse distance weighted (IDW) method was applied, as it yielded higher interpolation precision than other general methods when distributing the solar radiation spatial pattern in China [49]. The background theory and specific calculations steps of the IDW are detailed in the study by Goovaerts [50].

2.5. Intensity Analysis. The intensity analysis method developed by Aldwaik and Pontius [37] fully utilized a transition matrix to quantitatively analyze the intensity of land use and land cover changes at three distinct levels (time interval, land class hierarchy, and conversion) during different time periods [37]. Similarly, the solar radiation within the different levels in the study region was also usually dynamically changing during the different periods. The intensity analysis method was introduced to counter these dynamic changes and to address three problems on spatiotemporal variation in solar radiation. (1) Is the total annual change of solar radiation occurring quickly or slowly within a certain time period? Formulas (8) and (9) were used to answer this problem. (2) Based on the previous answer, does the solar radiation at different levels vary gently or actively? Formulas (10) were used to answer this problem. (3) Based on the two former answers, which conversion form dominated the process of mutual transition between different levels of solar radiation? Formulas (11)–(14) were used to answer this problem. By addressing these three problems, the overall tendency of solar radiation, the dynamic change regulations of solar radiation at different levels, and the mutual conversion regularity between different levels across NEC were revealed.

The specific calculations of intensity analysis are shown in formulas (8)–(14):

$$U = \frac{\left\{\sum_{t=1}^{T-1}\left[\left(\sum_{i=1}^{J} C_{tij}\right) - C_{tjj}\right]\right\} / \left[\sum_{j=1}^{J}\left(\sum_{i=1}^{J} C_{tij}\right)\right]}{Y_T - Y_1} \times 100\%, \tag{8}$$

$$S_t = \frac{\left\{\sum_{j=1}^{J}\left[\left(\sum_{i=1}^{J} C_{tij}\right) - C_{tjj}\right]\right\} / \left[\sum_{j=1}^{J}\left(\sum_{i=1}^{J} C_{tij}\right)\right]}{Y_{t+1} - Y_t} \times 100\%, \tag{9}$$

where U and S_t refer to the uniform line value for the whole time interval and the annual variation intensity for a certain time interval, respectively. J and T represent the solar radiation level and the number of points in time, respectively. The subscript indexes i and j henceforth stand for the solar radiation levels at the initial and final times for a certain time interval, respectively, and subscript index t henceforth indicates a certain point in time ranging from 1 to $T - 1$. Y_t henceforth denotes the year of t, and C_{tij} henceforth means the number of pixels transferred from the Y_t year at level i to the point in time Y_{t+1} at level j.

$$\begin{aligned} G_{tj} &= \frac{\left[\left(\sum_{i=1}^{J} C_{tij}\right) - C_{tjj}\right] / \left(Y_{t+1} - Y_t\right)}{\sum_{i=1}^{J} C_{tij}} \times 100\%, \\ L_{ti} &= \frac{\left[\left(\sum_{j=1}^{J} C_{tij}\right) - C_{tii}\right] / \left(Y_{t+1} - Y_t\right)}{\sum_{j=1}^{J} C_{tij}} \times 100\%. \end{aligned} \tag{10}$$

In the above formulas, G_{tj} and L_{ti} are the annual total increasing and decreasing intensity level j and level i during the time interval $[Y_t, Y_{t+1}]$, respectively.

$$W_{tn} = \frac{\left[\left(\sum_{i=1}^{J} C_{tin}\right) - C_{tnn}\right] / \left(Y_{t+1} - Y_t\right)}{\sum_{j=1}^{J}\left[\left(\sum_{i=1}^{J} C_{tij}\right) - C_{tnj}\right]} \times 100\%. \tag{11}$$

Here, W_{tn} refers to the uniform intensity of conversion from non-n levels at time point Y_t to level n during the time interval $[Y_t, Y_{t+1}]$, and subscript index n refers to the solar radiation level converted from other levels.

$$R_{tin} = \frac{C_{tin} / \left(Y_{t+1} - Y_t\right)}{\sum_{j=1}^{J} C_{tij}} \times 100\%. \tag{12}$$

In this formula, R_{tin} refers to the annual conversion intensity from level i to level n $(i \neq n)$ during the time interval $[Y_t, Y_{t+1}]$.

$$V_{tm} = \frac{\left[\left(\sum_{j=1}^{J} C_{tmj}\right) - C_{tmm}\right] / \left(Y_{t+1} - Y_t\right)}{\sum_{j=1}^{J}\left[\left(\sum_{j=1}^{J} C_{tij}\right) - C_{tim}\right]} \times 100\%. \tag{13}$$

In formula (13), V_{tm} refers to the uniform intensity of conversion from level m at time point Y_{t+1} to non-m levels during the time interval $[Y_t, Y_{t+1}]$, and subscript index m refers to the solar radiation level converting to other levels.

$$Q_{tmj} = \frac{C_{tmj} / \left(Y_{t+1} - Y_t\right)}{\sum_{j=1}^{J} C_{tij}} \times 100\%. \tag{14}$$

Table 2: Solar radiation classification in NEC.

Levels	Name	Classification threshold ($MJ \cdot m^{-2} \cdot a^{-1}$)
I	Abundant	$G^* \geq 5200$
II	Comparatively abundant	$5000 \leq G < 5200$
III	Normal	$4800 \leq G < 5000$
IV	Poor	$G < 4800$

* *Note*. G represents the annual total solar radiation.

Table 3: Statistic indicators of the BPNN and ACO-BPNN models.

Model	MAPE/%	MABE/$MJ \cdot m^{-2}$	RMSE/$MJ \cdot m^{-2}$	R
BPNN	6.49	23.68	35.60	0.9759
ACO-BPNN	6.45	23.03	31.45	0.9808

Table 4: Statistical indicators of the ACO-BPNN model at the verification stations.

Stations	MAPE/%	MABE/$MJ \cdot m^{-2}$	RMSE/$MJ \cdot m^{-2}$	R
SuoLun	4.54	17.2776	22.7772	0.9919
TongLiao	7.15	27.1159	38.5571	0.9729
ChangChun	4.50	14.7073	21.6252	0.9911

In the above, Q_{tmj} refers to the annual conversion intensity from level m to level j ($m \neq j$) during the time interval $[Y_t, Y_{t+1}]$.

In summation, the intensity analysis method was performed based on the distribution conditions of solar radiation at different levels at each point in time. Therefore, the classification criteria at all points in time must be uniform. In this study we used previous research to base the division of solar radiation resources across NEC [51, 52] and take the national current standard and specifications into consideration simultaneously. Finally, the solar radiation resources from 1982 to 2010 in NEC were divided into the four levels shown in Table 2, and the 1980s, 1990s, and 2000s were selected as the time points.

3. Results

3.1. Comparative and Validating Analysis of ACO-BPNN Model. A total of 5220 input/output pairs were employed to train the BPNN and ACO-BPNN to fully establish the relationship between the input vector $X = [\text{at, ws, vp, rh, ca, sd, dtr}]^T$ and the output vector $Y = [\text{solar radiation}]^T$ at 15 stations from 1982 to 2010. Following this, there was a performance comparison between the trained BPNN and ACO-BPNN using iteration times, network errors (E), and correlation coefficients (R).

As shown in Figure 4(a), an optimal solution was obtained after only five iterations through the ACO-BPNN model. However, the BPNN iterated 15 times to reach the convergence state, and the minimum network error was larger than the one obtained by ACO-BPNN. This indicated that the process of identifying an optimum solution by BPNN fell into the local optimal solution when modelling solar radiation. In addition to the rate of convergence, the MAPE, MABE, and RMSE of the ACO-BPNN were all less than the BPNN, and a higher correlation coefficient of observed and simulated monthly solar radiation was achieved by the ACO-BPNN (0.9808) than by BPNN (0.9759) (Table 3). Therefore, it was concluded that the modified ACO-BPNN performed superiorly to the traditional BPNN.

Although the optimized ACO-BPNN accurately characterized the complicated functional relationship between solar radiation and the independent variables, further testing was required before applying it to estimate solar radiation at other meteorological stations without radiation observations. To achieve this, the modified ACO-BPNN needed validation at other radiation stations where observed data did not contribute to its training process.

As shown in Figure 5, a total of three verification stations are reserved for testing, including SuoLun, TongLiao, and ChangChun; radiation observations are collected at these locations from 2000 to 2010. The contrast result reveals a strong fit between the observed and simulated values.

Table 4 lists the statistical error metrics and the model fit of the stations, where the MAPE was between 4.54% and 7.15%, the MABE ranged from 14.7073 $MJ \cdot m^{-2}$ to 27.1159 $MJ \cdot m^{-2}$, the RMSE varied from 21.6252 $MJ \cdot m^{-2}$ to 38.5571 $MJ \cdot m^{-2}$, and all the correlation coefficients of the modelled and observed values were greater than 0.97. This showed that the monthly solar radiation simulated by the ACO-BPNN achieved high accuracy.

Based on comparative and validating analysis of the ACO-BPNN model, it was determined that the ACO-BPNN model had superior performance in estimating solar radiation compared to traditional models and could be applied to other 96 weather stations lacking observations.

3.2. Spatial Patterns of Solar Radiation during Different Periods. Based on monthly solar radiation of 114 stations including 96 simulated weather stations and 18 observed radiation stations for the period 1982–2010, we obtained spatial patterns of solar radiation over NEC in the 1980s, 1990s, and 2000s

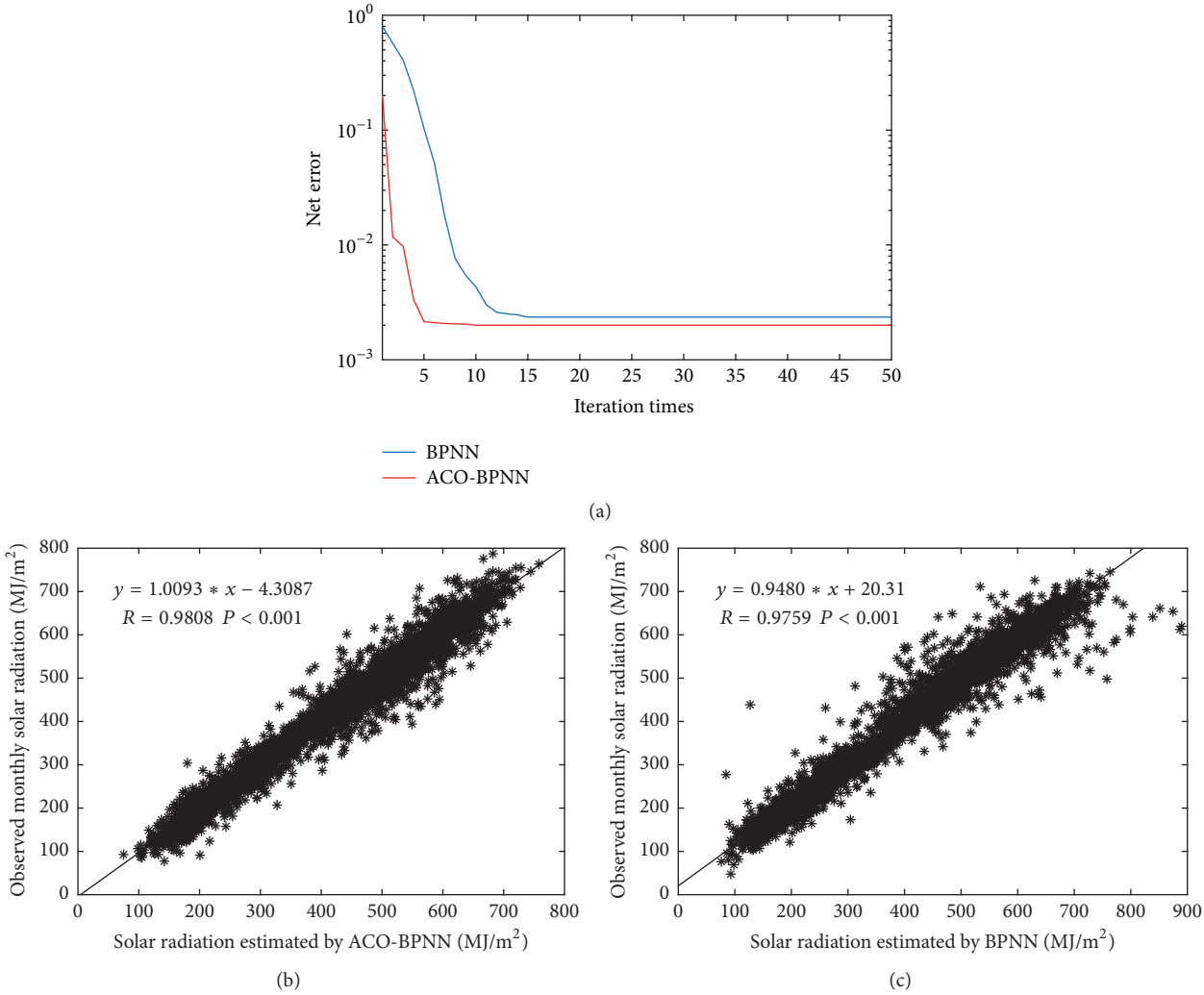

Figure 4: Performance comparison between BPNN and ACO-BPNN using network error, iteration times (a), and correlation coefficient ((b) and (c)).

by utilizing inverse distance weighting (IDW) interpolation method (Figure 6). This not only merged solar radiation information at each year into the corresponding decade but also satisfied the precondition of following intensity analysis.

On this basis, we classified solar radiation for different periods according to the established division standard (Table 2). As shown in Figure 7, higher levels of solar radiation resources appeared in the south and west of the study region, while lower ones occurred in the north and east. Overall, the solar radiation resources show a steady decreasing trend from the southwest to the northeast across the study region.

To acquire further detailed variations of solar radiation resources over NEC during the three periods, statistics on the areas of solar radiation resources at different levels during various time periods were calculated. The results in Table 5 highlight that the poor level area accounted for the largest proportion, while the area ratio of the abundant level was the smallest, and the area of normal and comparatively abundant levels accounted for the difference between the two from 1980s to 2000s. Compared to the 1980s, in the other decades the proportion of the normal level area was greater than the comparative level. The ratio of poor level area was more than 40% for all three periods, indicating that although the solar radiation resources presented an upward trend in recent years, the amount of resources was still relatively general overall.

3.3. Intensity Analysis of Spatiotemporal Dynamics of Solar Radiation. We analyzed the spatial pattern of solar radiation at each level, and the corresponding statistics results from 1982–2010 are reported in this section. The intensity analysis was introduced to analyze the dynamic changes of the solar radiation from three perspectives: time interval, category, and conversion. To achieve this, the ArcGIS software platform was used to obtain the solar radiation transition matrix at two time stages (the 1980s–1990s and 1990s–2000s), which was a prerequisite for intensity analysis. The transition matrix is displayed in Table 6.

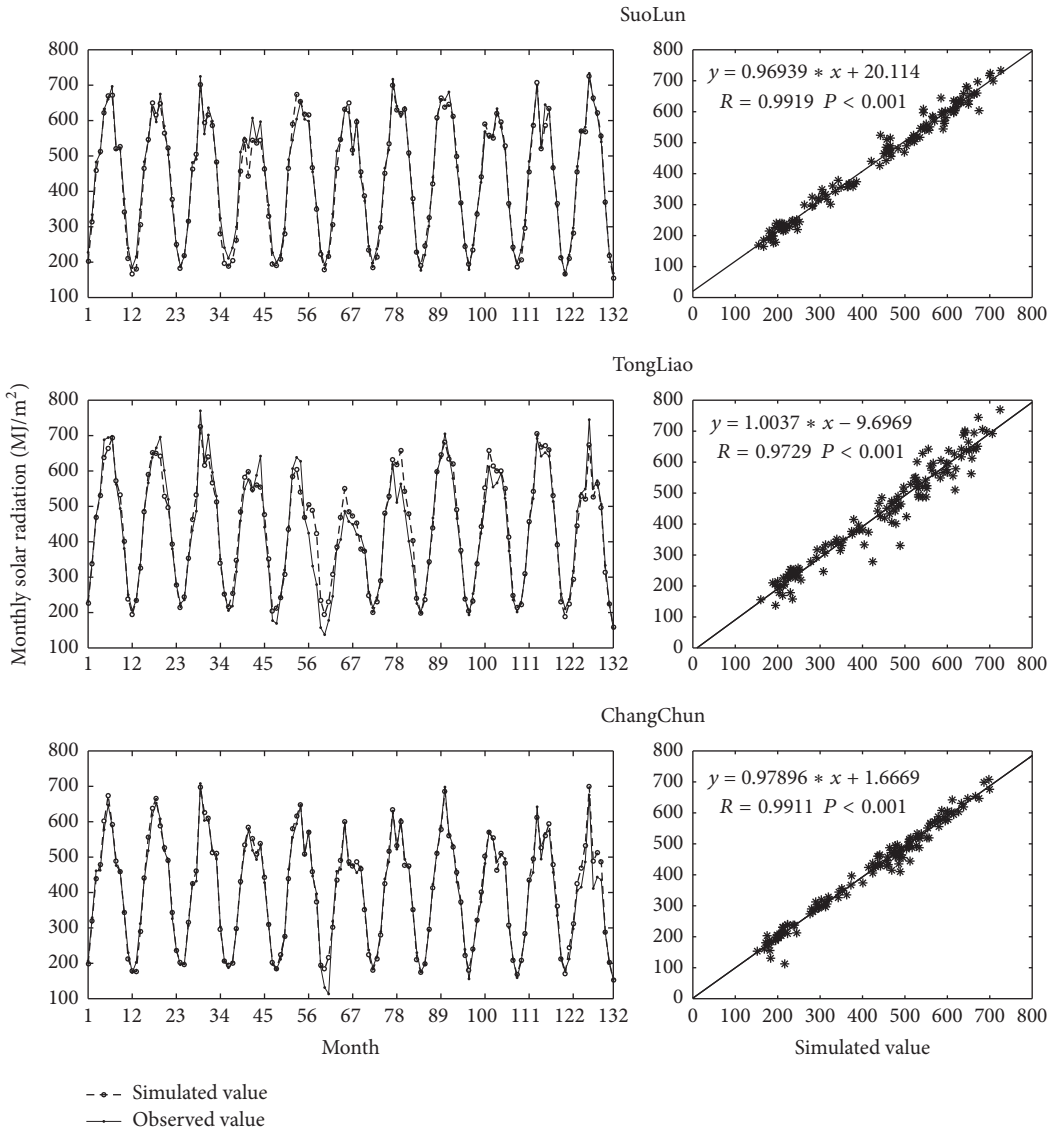

FIGURE 5: Comparison between observed and simulated values at SuoLun, TongLiao, and ChangChun from 2000 to 2010.

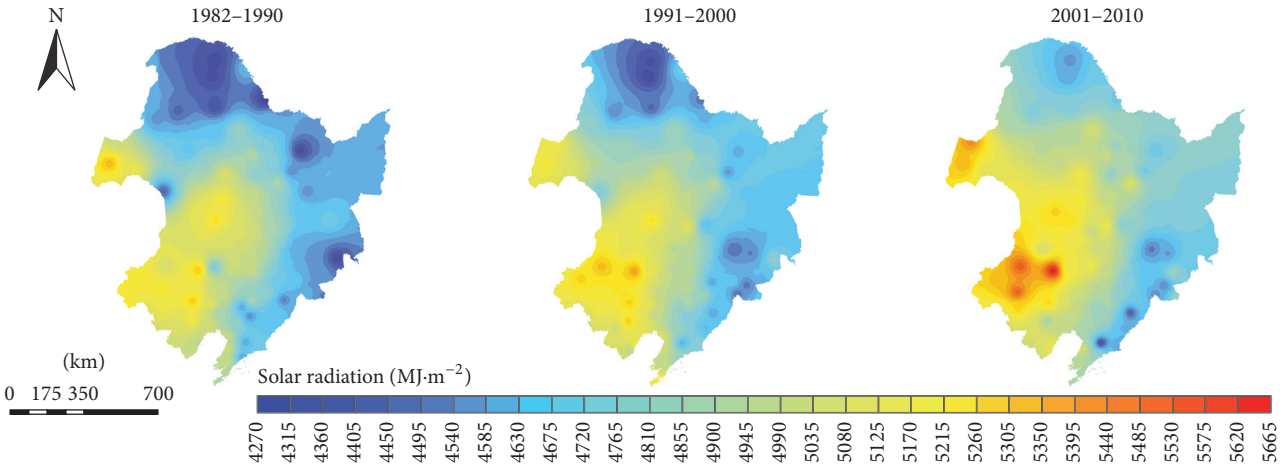

FIGURE 6: Spatial patterns of annual average solar radiation over Northeast China from 1982 to 2010.

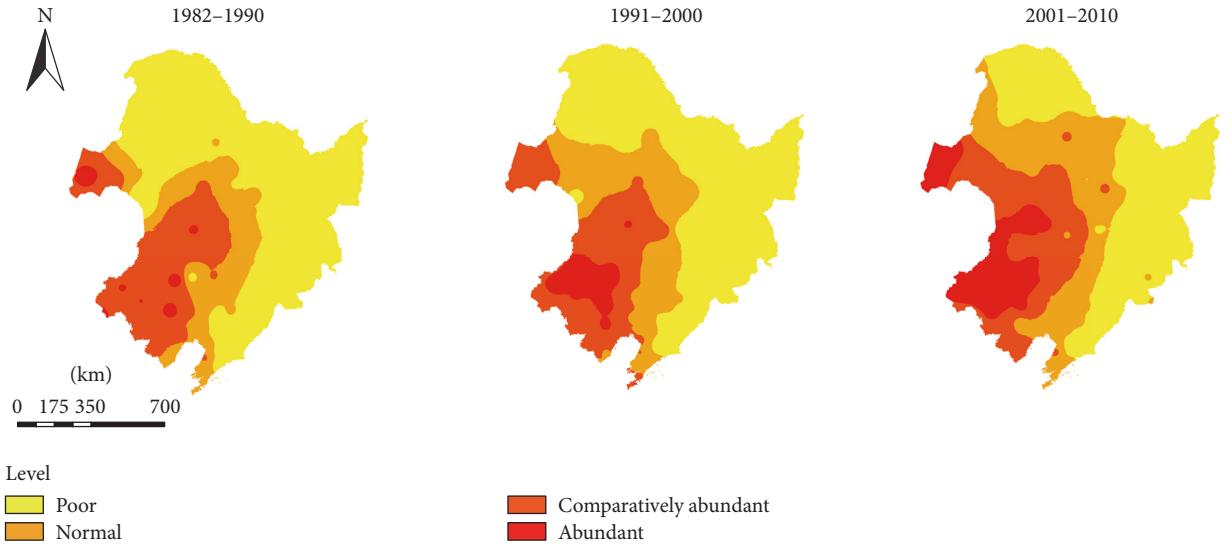

Figure 7: Spatial distribution of annual average solar radiation levels during the major temporal periods in Northeast China.

Table 5: Area statistics of vegetation coverage levels in each period.

Periods	Area & ratio	I	II	III	IV
1982–1990	Area (km^2)	18923	275287	222010	725953
	Ratio (%)	1.52%	22.16%	17.87%	58.44%
1991–2000	Area (km^2)	65289	256145	270977	649762
	Ratio (%)	5.26%	20.62%	21.81%	52.31%
2001–2010	Area (km^2)	155302	256224	327766	502881
	Ratio (%)	12.5%	20.63%	26.39%	40.48%
Variable area (km^2)	1980s–1990s	46366	−19142	48967	−76191
	1990s–2000s	90013	79	56789	−146881

Table 6: Transition matrix of different levels of solar radiation over two study periods (pixel).

	Terminal point					
	I	II	III	IV	Initiation	Gross loss
Initial point						
I	**8931**	**9992**	**0**	**0**	**18923**	**9992**
	60524	*2202*	*2563*	*0*	*65289*	*4765*
II	**56201**	**205098**	**13988**	**0**	**275287**	**70189**
	94778	*145262*	*16105*	*0*	*256145*	*110883*
III	**157**	**39718**	**165295**	**16840**	**222010**	**56715**
	0	*105535*	*160976*	*4466*	*270977*	*110001*
IV	**0**	**1337**	**91694**	**632922**	**725953**	**93031**
	0	*3225*	*148122*	*498415*	*649762*	*151347*
Gross gain	**56358**	**51047**	**105682**	**16840**		
	94778	*110962*	*166790*	*4466*		
Termination	**65289**	**256145**	**270977**	**649762**		
	155302	*256224*	*327766*	*502881*		

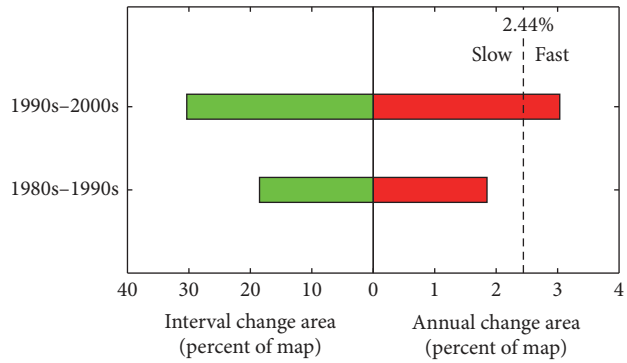

Figure 8: Time intensity analysis for the 1980s–1990s and 1990s–2000s over Northeast China.

The bold font refers to the variation of different levels of solar radiation from the 1980s to the 1990s, and the italicized font refers to the different solar radiation variation levels from the 1990s to the 2000s. On this basis, there is a further comprehensive analysis at the three levels consisting of time interval, category, and conversion for the table in the following sections.

3.3.1. Results of Time Interval Analysis. Figure 8 displays the analysis results for time intervals of solar radiation resources from the 1980s to the 2000s. The bars to the left of the central axis represent the overall intensity of solar radiation variation at each time interval. The bars right of the axis refer to time intensity calculated by formula (9). The dashed line on the right side was the uniform line acquired using formula (8). If the right-hand bar surpassed the uniform line, it was concluded that the variation of solar radiation resources levels at that time interval was comparatively fast. Otherwise, it meant that the variation was relatively slow.

As shown in Figure 8, there were notably more interval variations in solar radiation during the 1990s–2000s than in the 1980s–1990s. In addition, the rate of change in solar radiation from the 1990s to the 2000s was faster than that in the previous decade, as it passed the uniform line value (2.44%) for the whole period. Overall, regardless of the interval variations or changing rates, the solar radiation of the NEC region presented a tendency for growth.

The results of the time interval analysis provided general variations in the regularity of solar radiation resources during different periods, and the variation laws of solar radiation resources at different levels are outlined in the next section.

3.3.2. Results of Category Analysis. Figure 9 gives the results of the category analysis, which was used to identify whether the variation of solar radiation resources at different levels over two time intervals was active or gentle. Each pair of horizontal bars denotes a level of solar radiation resources. The bars on the right refer to the annual intensity gains and losses at each time period, which were obtained using formulas (10). The bars on the left refer to variation area (represented by pixel numbers) at each time period and were derived using the numerator of formulas (10). If the right-hand bar surpassed the uniform line (the dashed line) which was the output result of formula (9), it was confirmed that the variation of the solar radiation resources at that time stage was comparatively active. Otherwise, it meant that the variation was relatively stable.

The increasing and decreasing solar radiation conditions at each level from the 1980s to the 1990s are displayed in Figures 9(a1) and 9(a2). The results revealed that the increasing area of the abundant level was larger than its decreasing area, and the growing area of the normal level was slightly larger than its diminishing area. Conversely, the increasing area of the poor level was less than its decreasing area, and this was likewise for the comparatively abundant level. Moreover, in terms of the state of intensity variation, both the increases and decreases of the abundant level solar radiation were active. Unlike the abundant level, the comparatively abundant and normal level of solar radiation presented relatively active increases and decreases. Contrary to the former three levels, both the increases and decreases of the poor level solar radiation presented were minimal. Overall, the solar radiation resources in the 1990s were richer than in the 1980s.

Figures 9(b1) and 9(b2) show the result of the category analysis for the 1990s–2000s. The analysis revealed that the increasing area of abundant level was far larger than its decreasing area, and the growing area of comparatively abundant and normal level almost equalled their diminishing area. Unlike the former three levels, the increasing area of poor level was nearly zero, which was far less than its decreasing area. For the variation in intensity, the abundant level gains were fairly active, whereas its losses were relatively minimal; both the gains and losses of the comparatively abundant and normal levels were relatively active. In contrast, the poor level exhibited both gentle gains and losses. On the whole, the solar radiation resources of the 2000s were richer than the 1990s.

The category analysis not only confirmed the theory that the general intensity of solar radiation resources was increasing at an accelerated rate but also answered the question regarding the amount of activity variation between levels. However, the results regarding the mutual conversion relationships between solar radiation resources at each level were not involved and instead are presented in Section 3.3.3.

3.3.3. Results of Conversion Analysis. By comparing the conversion intensities of solar radiation resources from one level to other during each time interval, we identified which type of conversion was stronger. To achieve this goal, we summarized the dominant conversions for each time period according to the results of the category analyses obtained from formulas (11)–(14). As shown in Table 7, the leading form of solar radiation resources at each level during the 1980s–1990s was generally consistent with that from the 1990s–2000s. The poor, normal, and comparatively abundant levels converted to normal, comparatively abundant, and abundant levels, respectively. The abundant level predominantly converted into comparatively abundant and normal levels. In general, the poor, normal, and normal

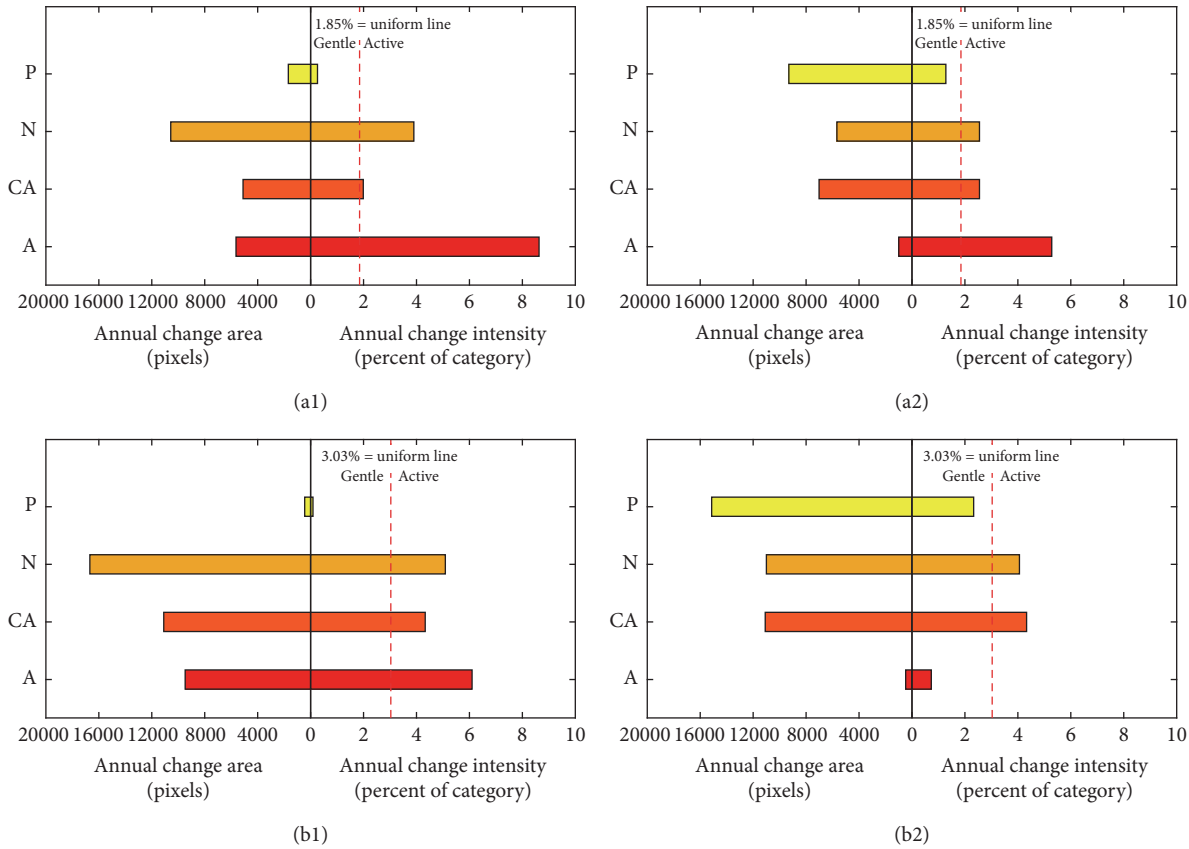

Figure 9: Category intensity analysis for the 1980s–1990s (a1, a2) and 1990s–2000s (b1, b2); (a1)/(b1) denote gains and (a2)/(b2) are losses; A, CA, N, and P represent the classifications abundant, comparatively abundant, normal, and poor.

Table 7: Conversion of dominant solar radiation in Northeast China in the 1980s–1990s and the 1990s–2000s.

Convert from	Convert into	
	1980s–1990s	1990s–2000s
Poor	Normal	Normal
Normal	Comparatively abundant	Comparatively abundant
Comparatively abundant	Abundant	Abundant
Abundant	Comparatively abundant	Comparatively abundant & normal

level resources mainly converted into higher levels, but the abundant level mainly converted to a lower level.

The conversion analysis further verified the result of the interval and category analysis and uncovered the conversion relationships between the different levels.

4. Discussion

4.1. Estimation of Solar Radiation. The reasons for variations in solar radiation are complicated, as the latter has complex coupling relationships with many meteorological factors. Therefore, the BPNN model can be applied to estimate solar radiation, as it is suitable for addressing fuzzy problems that require many factors and uncertainties to be considered. However, the traditional BPNN model also has some disadvantages; for example, if the initial values of set parameters are not appropriate, the optimization process easily generates default local minimums. To solve this problem and simulate more accurate monthly solar radiation values, we utilized an ACO algorithm to modify the traditional BPNN and constructed a new ACO-BPNN model. Our idea was to make full use of the global optimization ability of the ACO algorithm to provide several optimized groups of initial weighted values for the BPNN, to further refine the most appropriate weights for the BPNN, and finally to obtain an optimal global solution.

Comparative analysis revealed that when considering convergence speed and the network error, the improved ACO-BPNN had a superior performance to the BPNN model. Through further contrast and verification of the observed and simulated values, it was revealed that the modified ACO-BPNN had excellent generalization in the study area and could be used to estimate the solar radiation of other nonradiation data stations.

The ACO-BPNN developed in this study is a promising method for radiation prediction, especially for the remote regions without radiation observation, but there are possibilities for improvement in future studies. Namely, as the site data used in this study were discrete, solar radiation with continuous spatial distribution from remotely sensed data would be a desirable addition for the ACO-BPNN model.

4.2. Dynamic Intensity of Solar Radiation. In this study, the intensity analysis method was introduced into the dynamic study of solar radiation. Our research results revealed that, on the whole, the solar radiation over NEC had an obviously upward trend during the study period of 1980–2010, which was consistent with results of previous studies [44–46]. This estimated increasing trend was also in accordance with the findings of Wild et al. (2005), who deemed that the surface of the Earth has shifted from "dark" to "bright" over the past decade. Specifically, the solar radiation reaching the Earth's surface presented an overall increasing trend from the 1980s onwards, which indicated that the variation trend of solar radiation might have global characteristics [53].

The intensity analysis method was applied to deeply excavate the spatiotemporal variation of solar radiation across NEC from category and conversion aspects. Compared with previous trend, cycle, and principal component analysis methods based on station data, this study focused on the area of solar radiation at each level, which made a more detailed spatiotemporal analysis possible by considering both the variation and conversion of different levels of solar radiation. Nevertheless, there were still some shortcomings in the intensity analysis method that need to be further developed in future studies; one such example is the lack of locational information in the analysis process.

5. Conclusions

In this study, we first utilized the ACO-BPNN model modified by the ACO algorithm to simulate monthly solar radiation and then used IDW interpolation to acquire monthly spatial patterns based on the radiation data. This included simulated radiation of 96 stations and observed radiation of 18 stations from 1982 to 2010. Based on the results, the spatiotemporal variation of solar radiation resources over NEC was analyzed from the aspects of time interval, category, and conversion by intensity analysis. The main conclusions can be summarized as follows:

(1) The ACO-BPNN model outperformed the traditional BPNN, whether based on the network error and convergence rate or fit between simulation and observation, in all aspects. The contrast verification between simulated and observed solar radiation at the SuoLun, TongLiao, and ChangChun stations showed that the time series of simulated solar radiation were highly consistent with observed ones, which indicated that the ACO-BPNN we developed can be applied to model solar radiation in regions lacking radiation data.

(2) The solar radiation of the study region had a downward trend from the southwest to the northeast during the 1980s–2000s. In the 1980s, the areas of varying levels of solar radiation from large to small were as follows: the poor level, the comparatively abundant level, the normal level, and the abundant level. However, during the 1990s and 2000s, the area of solar radiation at each level was in the following order: poor > normal > comparatively abundant > abundant. Overall, the solar radiation resources in NEC continued to increase during the study period of 1980s–2000s.

(3) The annual average rate of variation of solar radiation during the 1980s–1990s was lower than that during the 1990s–2000s. From the 1980s–1990s, solar radiation was actively increasing and decreasing in abundance, and the abundant and normal levels exhibited relatively active increases and decreases whereas the variation level experienced comparatively gentle fluctuations. During the 1990s–2000s, the abundant level had active gains, but the losses were subtle. The increases and decreases of the comparatively abundant and normal levels were active. In contrast, the poor level showed a gentle increase and decrease. The poor, normal, and comparatively abundant levels were converted to higher levels, whereas the abundant level transformed to lower levels.

Conflicts of Interest

The authors declare no competing financial interests.

Acknowledgments

This study was supported by the Youth Program of National Natural Science Foundation of China (Grant no. 41201549).

References

[1] G. Wu, Y. Liu, and T. Wang, "Methods and strategy for modeling daily global solar radiation with measured meteorological data - A case study in Nanchang station, China," *Energy Conversion and Management*, vol. 48, no. 9, pp. 2447–2452, 2007.

[2] J. Almorox, C. Hontoria, and M. Benito, "Models for obtaining daily global solar radiation with measured air temperature data in Madrid (Spain)," *Applied Energy*, vol. 88, no. 5, pp. 1703–1709, 2011.

[3] F. Besharat, A. A. Dehghan, and A. R. Faghih, "Empirical models for estimating global solar radiation: a review and case study," *Renewable and Sustainable Energy Reviews*, vol. 21, pp. 798–821, 2013.

[4] M. I. Budyko, "The effect of solar radiation variations on the climate of the Earth," *Tellus*, vol. 21, no. 5, pp. 611–619, 1969.

[5] J. Lean and D. Rind, "Climate forcing by changing solar radiation," *Journal of Climate*, vol. 11, no. 12, pp. 3069–3094, 1998.

[6] J. Boland, "Spatial-temporal forecasting of solar radiation," *Renewable Energy*, vol. 75, pp. 607–616, 2015.

[7] G. A. Saenz and H.-P. Huang, "Trends in downward solar radiation at the surface over north America from climate model projections and implications for solar energy," *Advances in Meteorology*, vol. 2015, Article ID 483679, 7 pages, 2015.

[8] E. Zell, S. Gasim, S. Wilcox et al., "Assessment of solar radiation resources in Saudi Arabia," *Solar Energy*, vol. 119, pp. 422–438, 2015.

[9] L. Bechini, G. Ducco, M. Donatelli, and A. Stein, "Modelling, interpolation and stochastic simulation in space and time of

global solar radiation," *Agriculture, Ecosystems and Environment*, vol. 81, no. 1, pp. 29–42, 2000.

[10] C. A. Gueymard, *A simple Model of the Atmospheric Radiative Transfer of Sunshine: Algorithm and performance assessment FSEC-PF-270-95*, Florida Solar Energy Center/University of Central Florida.

[11] C. A. Gueymard, "REST2: High-performance solar radiation model for cloudless-sky irradiance, illuminance, and photosynthetically active radiation - Validation with a benchmark dataset," *Solar Energy*, vol. 82, no. 3, pp. 272–285, 2008.

[12] B. E. Psiloglou and H. D. Kambezidis, "Performance of the meteorological radiation model during the solar eclipse of 29 March 2006," *Atmospheric Chemistry and Physics*, vol. 7, no. 23, pp. 6047–6059, 2007.

[13] H. D. Kambezidis and B. E. Psiloglou, "The meteorological radiation model (MRM): Advancements and applications," in *Modeling Solar Radiation at the Earth's Surface: Recent Advances*, pp. 357–392, 2008.

[14] H. D. Kambezidis, B. E. Psiloglou, D. Karagiannis, U. C. Dumka, and D. G. Kaskaoutis, "Recent improvements of the Meteorological Radiation Model for solar irradiance estimates under all-sky conditions," *Renewable Energy*, vol. 93, pp. 142–158, 2016.

[15] H. Kambezidis, B. Psiloglou, D. Karagiannis, U. Dumka, and D. Kaskaoutis, "Meteorological Radiation Model (MRM v6.1): Improvements in diffuse radiation estimates and a new approach for implementation of cloud products," *Renewable and Sustainable Energy Reviews*, vol. 74, pp. 616–637, 2017.

[16] M. A. Atwater and J. T. Ball, "A numerical solar radiation model based on standard meteorological observations," *Solar Energy*, vol. 21, no. 3, pp. 163–170, 1978.

[17] J. A. Davies and D. C. McKay, "Evaluation of selected models for estimating solar radiation on horizontal surfaces," *Solar Energy*, vol. 43, no. 3, pp. 153–168, 1989.

[18] C. Gueymard, "A two-band model for the calculation of clear sky solar irradiance, illuminance, and photosynthetically active radiation at the earth's surface," *Solar Energy*, vol. 43, no. 5, pp. 253–265, 1989.

[19] B. E. Psiloglou, M. Santamouris, and D. N. Asimakopoulos, "Atmospheric broadband model for computation of solar radiation at the earth's surface. Application to mediterranean climate," *Pure and Applied Geophysics*, vol. 157, no. 5, pp. 829–860, 2000.

[20] C. A. Gueymard, "Clear-sky irradiance predictions for solar resource mapping and large-scale applications: Improved validation methodology and detailed performance analysis of 18 broadband radiative models," *Solar Energy*, vol. 86, no. 8, pp. 2145–2169, 2012.

[21] K. L. Bristow and G. S. Campbell, "On the relationship between incoming solar radiation and daily maximum and minimum temperature," *Agricultural and Forest Meteorology*, vol. 31, no. 2, pp. 159–166, 1984.

[22] D. L. Liu and B. J. Scott, "Estimation of solar radiation in Australia from rainfall and temperature observations," *Agricultural and Forest Meteorology*, vol. 106, no. 1, pp. 41–59, 2001.

[23] T. C. Chineke, "Equations for estimating global solar radiation in data sparse regions," *Renewable Energy*, vol. 33, no. 4, pp. 827–831, 2008.

[24] J. Mubiru and E. J. K. B. Banda, "Estimation of monthly average daily global solar irradiation using artificial neural networks," *Solar Energy*, vol. 82, no. 2, pp. 181–187, 2008.

[25] S. Rehman and M. Mohandes, "Artificial neural network estimation of global solar radiation using air temperature and relative humidity," *Energy Policy*, vol. 36, no. 2, pp. 571–576, 2008.

[26] M. Benghanem, A. Mellit, and S. N. Alamri, "ANN-based modelling and estimation of daily global solar radiation data: A case study," *Energy Conversion and Management*, vol. 50, no. 7, pp. 1644–1655, 2009.

[27] D. A. Fadare, "Modelling of solar energy potential in Nigeria using an artificial neural network model," *Applied Energy*, vol. 86, no. 9, pp. 1410–1422, 2009.

[28] M. Espadafor, I. J. Lorite, P. Gavilán, and J. Berengena, "An analysis of the tendency of reference evapotranspiration estimates and other climate variables during the last 45 years in Southern Spain," *Agricultural Water Management*, vol. 98, no. 6, pp. 1045–1061, 2011.

[29] R. Salomon and J. L. Van Hemmen, "Accelerating backpropagation through dynamic self-adaptation," *Neural Networks*, vol. 9, no. 4, pp. 589–601, 1996.

[30] M. Gevrey, I. Dimopoulos, and S. Lek, "Review and comparison of methods to study the contribution of variables in artificial neural network models," *Ecological Modelling*, vol. 160, no. 3, pp. 249–264, 2003.

[31] Y. Shen, Z. Zhao, and G. Shi, "The Progress in Variation of Surface Solar Radiation, Factors and Probable Climatic Effects," *Advances in Earth Science*, vol. 23, no. 9, pp. 915–923, 2008.

[32] Z. Shen and H. Zhang, "Analysis on the factors affecting surface solar radiation and its spectral distribution," *Acta Energiae Solaris Sinica*, vol. 30, no. 10, pp. 1209–1215, 2009.

[33] S. Yang, K. Wang, and S. Lu, "Regional characteristics of global solar radiation evolution in china over recent 40 years," *Acta Energiae Solaris Sinica*, vol. 28, no. 3, pp. 227–232, 2007.

[34] O. E. Granger, "Climatology of global solar radiation in California and an interpolation technique based on orthogonal functions," *Solar Energy*, vol. 24, no. 2, pp. 153–168, 1980.

[35] F. Uno, T. Iizumi, M. Nishimori, and Y. Hayashi, "Time trends and variations in mean and accumulated solar radiation for the ripening period of paddy rice in Kyushu for 1979-2007," *Journal of Agricultural Meteorology*, vol. 68, no. 1, pp. 69–76, 2012.

[36] A. Peled and J. Appelbaum, "Evaluation of solar radiation properties by statistical tools and wavelet analysis," *Renewable Energy*, vol. 59, pp. 30–38, 2013.

[37] S. Z. Aldwaik and R. G. Pontius, "Intensity analysis to unify measurements of size and stationarity of land changes by interval, category, and transition," *Landscape and Urban Planning*, vol. 106, no. 1, pp. 103–114, 2012.

[38] H. Zheng and J. Liu, "Long-term trends of aridity index and its sensitivity to climate factors in Northeast China," *Geographical Research*, vol. 30, no. 10, pp. 1765–1774, 1971.

[39] Z. Liu, X. Yang, K. G. Hubbard, and X. Lin, "Maize potential yields and yield gaps in the changing climate of northeast China," *Global Change Biology*, vol. 18, no. 11, pp. 3441–3454, 2012.

[40] L. Hui, F. Yao, J. Zhang, and C. Hao, "Analysis on Climatic Maize Yield and Its Sensitivity to Climate Change in Northeast China," *Chinese Journal of Agrometeorology*, vol. 35, no. 4, pp. 423–428, 2014.

[41] Y. Xu, J. Qiao, X. Hou, and S. Pan, "Plutonium in soils from northeast China and its potential application for evaluation of soil erosion," *Scientific Reports*, vol. 3, article 3506, 2013.

[42] R. Huang and D. H. Yan, "Spatiotemporal evolution of the drought and flood in northeast China," *Advanced Materials Research*, vol. 1010-1012, pp. 1075–1083, 2014.

[43] X. Y. Yu, X. Y. He, H. H. Zheng et al., "Spatial and temporal analysis of drought risk during the crop-growing season over northeast China," *Natural Hazards*, vol. 71, no. 1, pp. 275–289, 2014.

[44] Z. Wu, H. Du, D. Zhao, M. Li, X. Meng, and S. Zong, "Estimating daily global solar radiation during the growing season in Northeast China using the Ångström-Prescott model," *Theoretical and Applied Climatology*, vol. 108, no. 3-4, pp. 495–503, 2012.

[45] J. Xie, T. Zhang, M. Zhang, and H. Zhang, "Change and reason analysis of ground solar radiation in Northeast China over recent 50 years," *Acta Energiae Solaris Sinica*, vol. 33, no. 12, pp. 2127–2134, 2012.

[46] Q. Hu, F. Pan, X. Pan et al., "Trends in agricultural heat and solar radiation resources in Northeast China: a multistage spatiotemporal analysis," *International Journal of Climatology*, vol. 36, no. 6, pp. 2461–2468, 2015.

[47] R. Hecht-Nielsen, "Theory of the backpropagation neural network," in *Proceedings of the International Joint Conference on Neural Networks (IJCNN '89)*, vol. 1, pp. 593–605, Washington, DC, USA, June 1989.

[48] M. Dorigo, V. Maniezzo, and A. Colorni, "Ant system: optimization by a colony of cooperating agents," *IEEE Transactions on Systems, Man, and Cybernetics B: Cybernetics*, vol. 26, no. 1, pp. 29–41, 1996.

[49] M. Mai, Y. Huo, and Y. Yu, "Comparison of interpolation scheme for solar radiation empirical coefficient," *Journal of Meteorology and Environment*, vol. 27, no. 5, pp. 42–45, 2011.

[50] P. Goovaerts, "Geostatistical approaches for incorporating elevation into the spatial interpolation of rainfall," *Journal of Hydrology*, vol. 228, no. 1-2, pp. 113–129, 2000.

[51] Q. Gong, "Temporal-Spatial Distribution and Regionalization of Wind and Solar Energy Resources in Liaoning Province," *Resources Science*, vol. 30, no. 5, pp. 654–661, 2008.

[52] H. Yu, N. Lin, and Y. Yu, "Solar energy resource distribution and regional division in Liaoning province," *Journal of Meteorology and Environment*, vol. 24, no. 2, pp. 18–22, 2008.

[53] M. Wild, H. Gilgen, A. Roesch et al., "From dimming to brightening: decadal changes in solar radiation at earth's surface," *Science*, vol. 308, no. 5723, pp. 847–850, 2005.